

Development of a water based process for stable conversion cathodes on the basis of FeF₃

Alexander Pohl^{*,a}, Andreas Schröder^{a,b}, Michael Baunach^b, Saman Faraz^a, Alexander Guda^c, Viktor Shapovalov^c, Kiran Chakravadhanula^d, Ralf Witte^a, Thomas Diemant^e, Herman Emerich^f and Maximilian Fichtner^{a,d}

^a Institute of Nanotechnology, Karlsruhe Institute of Technology, P.O. Box 3640, 76021 Karlsruhe, Germany

^b Institute of Thermal Process Engineering, Thin Film Technology, Karlsruhe Institute of Technology, P.O. Box 3640, 76021 Karlsruhe, Germany

^c International Research Center "Smart Materials", Southern Federal University, 5 Zorge St., 344090 Rostov-on-Don, Russian Federation

^d Helmholtz Institute Ulm (HIU), Helmholtzstr. 11, 89081 Ulm, Germany.

^e Institute of Surface Chemistry and Catalysis, Ulm University, Albert-Einstein-Allee 47, 89069 Ulm, Germany

^f Swiss-Norwegian Beamline, European Synchrotron Radiation Facility, BP 220, 38043 Grenoble, France

*corresponding author: alexander.pohl@kit.edu

Fax: +49 721 608 28298; Tel: +49 721 608 26377

Abstract

A facile water based synthesis method for HTB-FeF₃/rGO and *r*-FeF₃/rGO composites was developed using FeF₃ nanoparticles prepared by ball-milling and aqueous graphene oxide precursor. Electrodes of HTB-FeF₃/rGO were cast in ambient air and the calendared electrode showed a stable specific energy of 470 Wh kg⁻¹ (210 mAh g⁻¹, 12 mA g⁻¹) after 100 cycles in the range 4.3-1.3 V with very little capacity fading. The good cycle stability is attributed to the intimate contact of FeF₃ nanoparticles with reduced graphene oxide carbon surrounding. We show using a combination of *in situ* XRD, XAS and *ex situ* Mössbauer spectroscopy that during discharge of HTB-FeF₃/rGO composite Li is intercalated fast into the tunnels of the HTB-FeF₃ structure up to $x = 0.95$ Li followed by slow conversion to LiF and Fe nanoparticles below 2.0 V. During charge, the LiF and Fe phases are slowly transformed to amorphous FeF₂ and FeF₃ phases without reformation of the HTB-FeF₃ framework structure. At an elevated temperature of 55 °C a much higher specific energy of 780 Wh kg⁻¹ was obtained.

Introduction

The energy density (gravimetric and volumetric) of fossil fuels such as gasoline, diesel and, when extracted from natural gas also hydrogen, is about 50-100 times higher than that of current Li-ion, NiMH and lead acid batteries.¹ This explains why it is tremendously difficult to develop full cell battery electric vehicles (BEV's), which have the same or nearly the same driving range (800-1200 km) than that of traditional automobiles based on the internal combustion engine. Recently, the US department of energy has defined a new target for electrochemical storage devices for automotive applications.² For a car to reach a driving range of 300 miles (ca. 480 km), the battery needs to have an energy density of 250 Wh kg⁻¹ at system level, which is 2.5 times higher than state-of-the-art battery packs currently in use for BEV's.³ After taking losses related to the electrode formulation (binder, carbon additives), electrode casting (thickness of active layer and current collector, porosity), cell construction (prismatic, pouch or round) and battery stack assembly (battery management, cooling etc.) into account, the electrode material is required to have a practical energy density of 700-800 Wh kg⁻¹ at high C-rates.

Conversion materials, with the general formula $M^{n+}X_n + n \cdot e^- + n \cdot Li^+ \rightleftharpoons M^0 + n \cdot LiX$ and the ability to transfer more than one electron per transition metal ($n > 1$), are considered as next generation high capacity cathode materials.^{3,4} In a conversion material, M is usually a 3d transition metal and X^{n-} an anion such as H⁻, O²⁻, F⁻, S²⁻ and Se²⁻.⁵ The battery is usually constructed in the charged state and on discharge, the metal fluoride, metal oxide etc. is transformed into metal nanoparticles M⁰ dispersed in an insulating matrix of LiX.⁶ Conversion materials based on metal fluorides are particularly interesting, because of the strong M-F bond, some of them such as FeF₃, CoF₃, NiF₃ and CuF₂ have a high operating voltage (> 2.5 V) suitable as cathodes.⁷ Iron fluoride is particularly interesting because it has the highest theoretical energy density of 1950 Wh kg⁻¹ (2.74 V, 712 mAh g⁻¹) and is non-toxic, environmentally friendly, cheap and abundant.⁸

Traditionally, FeF₃/C composites have been prepared by ball-milling commercial rhombohedral *r*-FeF₃ with carbon black to reduce the primary particle size and to coat the *r*-FeF₃ nanoparticles with an electrically conducting layer of carbon.⁹ This approach leads to materials with large initial capacity up to the theoretical maximum of 712 mAh g⁻¹, but poor cycle stability as the carbon coating is incomplete and not attached strongly enough to the FeF₃ particle surface. The carbon shell "peels off" during prolonged cycling due to pulverisation of the electrode (repeated formation of Fe/LiF phases). To improve cycle stability, graphene oxide has been recently utilised in a number of publications to enable *r*-FeF₃/rGO composite materials with strong FeF₃/carbon interactions.^{8,10-14} For example, Liu et al.¹¹ have prepared a *r*-FeF₃/rGO composite consisting of *in-situ* grown FeF₃·3H₂O anchored on HF-etched graphene sheets. After removal of water, the *r*-FeF₃/rGO composite shows a

remarkably high capacity of 210 mAh g⁻¹ when cycled between 2.0 and 4.5 V (C/5) and 490 mAh g⁻¹ when cycled in the range 1.5-4.5 V (C/10). The good cycle performance of this composite can be attributed to the high electronic conductivity and the low ionic resistance of the graphene sheets. Using a facile self-assembly approach, Zhao et al.¹⁰ have prepared free-standing *r*-FeF₃/rGO paper from FeF₃ nanoparticles and graphene oxide water suspension followed by photothermal reduction. The ability to self-assemble the *r*-FeF₃/rGO paper was attributed to attracting forces of FeF₃ nanoparticles, which are strongly hydrophilic and have a positive surface charge (zeta potential = 34(1) mV) and negatively charged graphene oxide suspension (zeta potential = -57(5) mV). The free-standing *r*-FeF₃/rGO paper used directly as cathode shows initial high capacity of 587 mAh g⁻¹ (20 mA g⁻¹), but cycle stability is poor with quick capacity fading after 20 cycles due to the special architecture of the free-standing *r*-FeF₃/rGO paper.

Iron-fluoride based nanomaterials with orthorhombic hexagonal-tungsten-bronze (HTB) structure were reported by Li and co-workers¹⁵⁻¹⁹ and prepared using a non-aqueous approach in an ionic liquid medium. The HTB-FeF₃·0.33H₂O material shows an interesting sponge-like morphology with needles on the surface and high Li-ion mobility. When considered as Li-intercalation host, HTB-FeF₃·0.33H₂O can store up to 0.66 Li per formula unit (156 mAh g⁻¹) and a reversible capacity of 130 mAh g⁻¹ was observed in the range 1.6-4.5 V.¹⁵ The stability of the HTB-FeF₃·0.33H₂O framework structure towards Li insertion was attributed to the presence of zeolitic water in the channels.

In this work, we developed a facile water based synthesis method to produce HTB-FeF₃/rGO (and *r*-FeF₃/rGO) nanocomposites using aqueous graphene oxide suspension and FeF₃ nanoparticles. The detailed charge/discharge mechanism in HTB-FeF₃/rGO was investigated using simultaneous *in situ* X-ray absorption spectroscopy (XAS) above the Fe K-edge, X-ray diffraction (XRD) and *ex-situ* Mössbauer spectroscopy. The combination of such methods determines unambiguously the charge state of Fe, the cycle life of initial crystalline HTB-FeF₃ phase and the Fe local surrounding.^{20,21}

Experimental

Synthesis of graphene oxide: Graphene oxide (GO) was used as a precursor for FeF₃/rGO composite materials and prepared from natural graphite flakes using a modified Hummer's method as described previously.¹⁰ For BET and SEM analysis, a fine GO powder was obtained by heating the GO suspension in NaOH followed by treatment in HCl as described in Dreyer *et al.*²²

Synthesis of HTB-FeF₃/rGO and *r*-FeF₃/rGO composites: The FeF₃/rGO composite materials were prepared by using ball milled commercial *r*-FeF₃ (Sigma-Aldrich, 98 %) and aqueous GO suspension followed by thermal reduction. Depending on the synthesis conditions, a mixture of HTB-FeF₃ and *r*-

FeF₃ polymorphs were obtained (Table 1). Details of the synthesis procedure can be found in the supplement.

Physical characterisation: The elemental concentrations of Fe and S were determined using inductive coupled plasma-optical emission spectroscopy (ICP-OES). Laboratory powder X-ray diffraction patterns were collected using a STOE Stadi P diffractometer equipped with a Dectris Mythen 1K linear silicon strip detector and Ge(111) double crystal monochromator (Mo K_{α1}, λ = 0.7093 Å) in Debye-Scherrer geometry. Samples were filled into 0.7 mm borosilicate capillaries and data was collected between 3-63 °2θ. The mass fractions of crystalline phases were determined by the Rietveld method using the TOPAS academic software.²³ Mössbauer spectra were recorded using a constant acceleration-type spectrometer in transmission geometry with a moving source of ⁵⁷Co in a Rh matrix. Approximately 50 mg material was sealed into a plastic bag inside an argon filled glove box. The isomer shift is given relative to α-Fe at room temperature.

Morphological characterisation: SEM micrographs were recorded at 10 kV using a Zeiss Leo-1530 scanning electron microscope (InLens detector) equipped with an Oxford Instruments X-max^N EDX detector. TEM characterisation was carried out using an aberration corrected FEI Titan 80-300 transmission electron microscope equipped with a Gatan imaging filter (Tridiem 863) operated at 80 kV. Samples were prepared by dispersing a small amount of powder onto holey carbon Au grids (Quantifoil) inside an argon filled glove box and transferred under Ar to the sample chamber using a Gatan vacuum transfer holder.

Electrochemical characterisation: Galvanostatic charge/discharge experiments of FeF₃/rGO cathodes versus Li-metal anode were performed using Swagelok-type cells and CR2032 coin cells. For Swagelok cells, the powders were mixed with 10 wt.% carbon black and used directly without casting. For coin cells, a slurry was prepared and the material cast onto Al foil. Details of the electrode preparation are given in the supplement.

In situ XAS/XRD characterisation: Simultaneous X-ray absorption spectra and diffraction patterns were recorded *in situ* at the Swiss-Norwegian Beamline (BM01B) of the European Synchrotron Radiation Facility (ESRF), Grenoble, France. The home-built battery cells with glassy carbon windows transparent for X-rays were constructed as described previously.²¹ Two cells were installed in parallel on a rotational stage and galvanostatic charge/discharge curves recorded using Gamry Interface 1000 potentiostats with a constant current of 50 μA. On each cell, diffraction was recorded for 15 minutes followed by Fe K-edge absorption for 20 minutes, then the stage was turned 180° for the other cell and data collection was resumed. Ten 2D diffraction images were recorded with 5 seconds acquisition time by the CMOS-Dexela 2D detector. Both the wavelength λ = 0.50574 Å and the

sample-to-detector distance of 324.05 mm were calibrated using LaB₆ and silicon powder standards. Subsequent averaging and integration were carried out using Fit2D software.²⁴ Fe K-edge X-ray absorption spectra were measured in transmission mode employing a Si(111) monochromator in continuous scanning mode. Ionization chambers were used to monitor intensity before and after sample and Fe foil was measured simultaneously with the sample as a reference compound to monitor possible energy drift.

Theoretical methods: The series of Fe K-edge XANES spectra collected at different voltages were mathematically decomposed into spectra representing phases formed during charge/discharge using principle component analysis (PCA)^{25,26} as implemented into FitIt software.²⁷ The concentrations of the components and spectra itself were determined using physical constraints: spectra should be normalized, the values of concentrations should be positive, two of three components under consideration should represent initial FeF₃ state and final Fe state of composite material.

Results and discussion

The HTB-FeF₃/rGO and *r*-FeF₃/rGO composites were synthesised using an aqueous graphene oxide water suspension and commercial FeF₃ as described in experimental section. Depending on the synthesis conditions (pre ball-milled vs. as received FeF₃, temperature, grinding vs. post ball-milling), the composites contained a mixture of rhombohedral FeF₃ and hexagonal-tungsten-bronze-type HTB-FeF₃ polymorphs with varying weight fractions and a small amount of WC (< 1 wt.%) introduced by abrasion during ball-milling process (Table 1). Using pre ball-milled nanocrystalline FeF₃, the majority of *r*-FeF₃ was transformed to HTB-FeF₃, whereas using the *r*-FeF₃ as received, the amount of HTB-FeF₃ in the composites was much less. The water based graphene oxide process is scalable, HF-free and a variable amount of reduced graphene oxide (rGO) carbon can be introduced by varying the amount and concentration of GO suspension. This is an advantage, as the optimal carbon content is fine-tuneable for production of a commercial material with an optimal electrical conductivity and gravimetric capacity. The HTB-FeF₃ structure has large hexagonal channels along the *c*-axis which can accommodate additional lattice water (Figure 1). Refinement of the O occupancy shows that the HTB-FeF₃.*x*H₂O phase in composites **(2)** and **(3)** is partially dehydrated with *x* = 0.28 **(2)** and *x* = 0.09 **(3)**, respectively. The removal of lattice water is also indicated by a slight contraction of the *a*-axis (5.3 % **(2)**, 3.5 % **(3)**) and expansion of the *c*-axis (1.1 % **(2)**, 2.0 % **(3)**).

Table 1: Synthesis conditions and Rietveld refinement parameters. Pre-BM: ball-milling of commercial FeF₃ before mixing with GO suspension, Post-BM: ball milling of composite material after manual grinding, reduction temperature and time, ICP-OES element concentrations of Fe and S, FeF₃ amount calculated from ICP-OES, *r*-FeF₃ and HTB-FeF₃ phase fractions from Rietveld refinement, refined oxygen occupancy and water content *x* in HTB-FeF₃.*x*H₂O and refined lattice parameters of main FeF₃ phase (literature data: *r*-FeF₃: *a* = 5.362 Å, α = 57.94°,²⁸ HTB-FeF₃.0.33H₂O: *a* = 7.423 Å, *b* = 12.730 Å, *c* = 7.526 Å)²⁹.

No.	pre-BM	post-BM	Temp. °C	Time h	Fe wt.%	S wt.%	FeF ₃ wt.%	<i>r</i> -FeF ₃ wt.%	HTB-FeF ₃ wt.%	O occ., xH ₂ O	Refined LP's Å, °
1	-	-	300	4	32.2	6.6	65.5	89(1)	11(1)	-	<i>a</i> : 5.3558(5) α : 58.098(7)
2	x	-	200	12	40.0	2.7	84.6	11.5(4)	88.5(4)	0.84(1), 0.28	<i>a</i> : 7.384(3) <i>b</i> : 12.780(5) <i>c</i> : 7.5339(5)
3	x	x	200	12	40.7	-	82.2	20.9(4)	77.1(4)	0.26(1), 0.09	<i>a</i> : 7.397(1) <i>b</i> : 12.761(2) <i>c</i> : 7.5412(6)

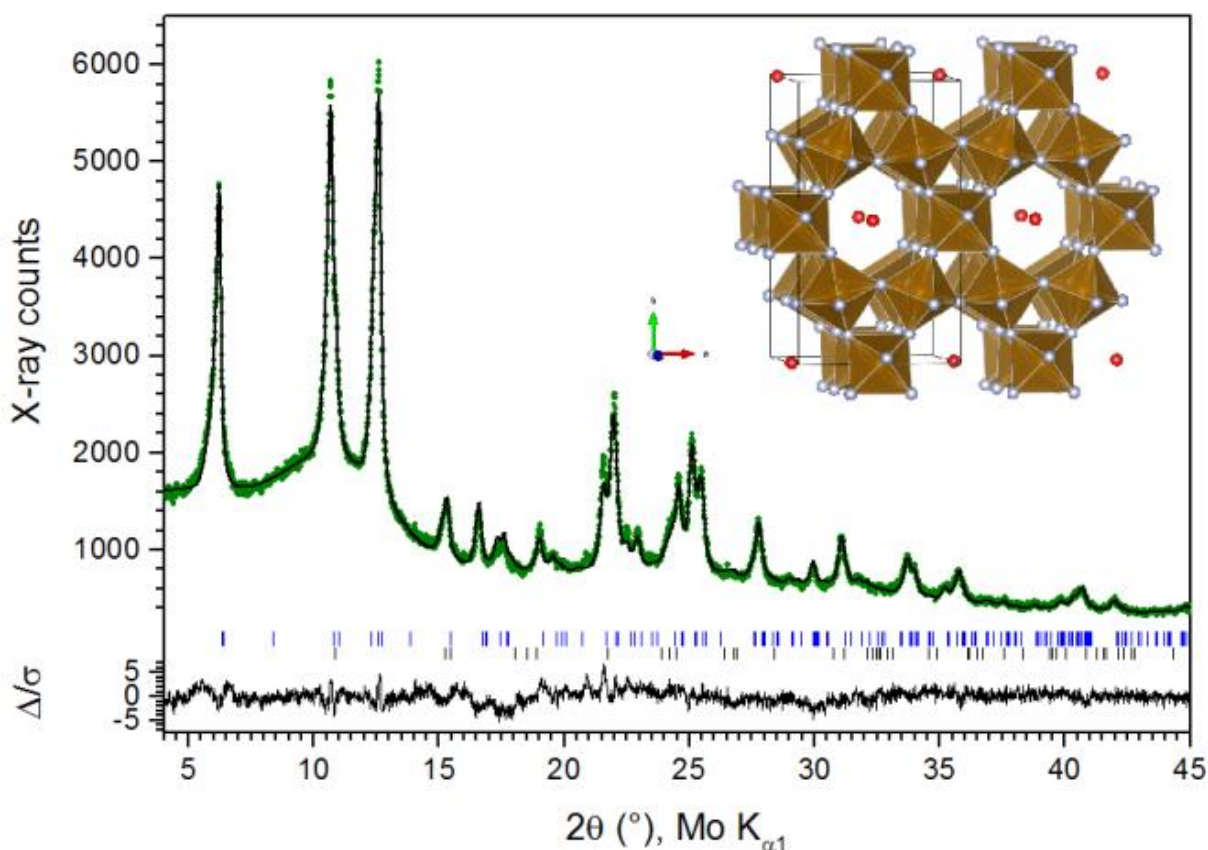


Figure 1: Rietveld refinement of HTB-FeF₃/rGO (2) composite ($\lambda = 0.7093$ Å). The green dots correspond to experimental data, the black line is the calculated fit. The blue and black tick marks are at the Bragg positions of HTB-FeF₃.0.28H₂O and *r*-FeF₃ phase, respectively. The inset shows the

the HTB-FeF₃ structure²⁹ with hexagonal tunnels along the *c*-axis filled 1/3 with water molecules (red spheres).

Electrochemical performance

The electrochemical performance of the composites (**1-3**) was found to be very similar after the first cycle irrespective of the amount of HTB-FeF₃ and *r*-FeF₃ polymorphs present. Electrodes of HTB-FeF₃/rGO (**2**) composite were prepared using a self-made batch coating machine with a custom designed slot nozzle dryer. The hygroscopic FeF₃ is well protected by the rGO carbon from ambient moisture enabling casting on the bench without affecting the performance of the electrode. This is beneficial as no special dry-room or inert gas conditions are required to produce high-quality, production-grade electrodes from these materials. The electrochemical performance of HTB-FeF₃/rGO (**2**) is shown in Figure 2. The composite was cycled at two different temperatures using as-cast and calendared electrodes. After the first few initial cycles the HTB-FeF₃/rGO composite shows excellent cycle stability compared to a *r*-FeF₃ composite prepared by ball milling with an equivalent amount of carbon black (HTB-FeF₃ (**2**): 22 wt.% rGO and extra CB, *r*-FeF₃: 30 wt.% CB). The as cast HTB-FeF₃/rGO electrode shows a stable discharge energy of 368 Wh kg⁻¹ (166 mAh g⁻¹, 12.8 mA g⁻¹, black curve) at 25°C for 100 cycles with negligible capacity fading after the 40th cycle. The stable cycle performance is attributed to a very firm contact of FeF₃ particles with the electron conducting reduced graphene oxide environment. The good contact is an effect of the attracting forces of the positively charged FeF₃ particle surface and negatively charged graphene oxide in water before drying.¹⁰ Calendaring the electrode increases the discharge energy by 29 % to 474 Wh kg⁻¹ (215 mAh g⁻¹, cycle 40-100, blue curve) without affecting the long term cycle stability due to pulverisation of small FeF₃ agglomerates present in the as cast electrode. Raising the temperature from 25°C to 40°C increases the specific energy also by 29 % to 473 Wh kg⁻¹ (222 mAh g⁻¹, 40-80 cycles, pink curve). The conversion rate of FeF₃ into LiF and Fe is accelerated due to higher ion mobility. However, after 80 cycles (not shown) the specific energy increases abnormally fast due to decomposition of the LiPF₆ electrolyte above 40°C.³⁰ Cycling the calendared electrode at 40 °C gives a specific energy increase of 59 % to 586 Wh kg⁻¹ (277 mAh g⁻¹, 40-60 cycles, red curve) compared to the as cast electrode cycled at 25°C.

Rate capability tests of as cast and calendared HTB-FeF₃ (**2**) electrodes were performed at two different temperatures and are shown in Figure 2b. The grey bar represents the specific energy target of 700-800 Wh kg⁻¹ required for practical automotive batteries.³ Both calendaring and the elevated temperature has a beneficial effect on the rate performance. The calendared electrode cycled at 55 °C shows a high average initial discharge energy of 900 Wh kg⁻¹ (435 mAh g⁻¹, 17 mA g⁻¹)

over cycles 2-4, which exceeds the target on materials level by 100-200 Wh kg⁻¹. When the current density is raised to 0.84 A g⁻¹ (equivalent to 1C), the discharged energy dropped considerably to 180 Wh kg⁻¹ (80 mAh g⁻¹). Compared to the fast Li-ion diffusion into the HTB-FeF₃ tunnel structure and other Li-intercalation host materials such as NMC, the conversion of HTB-Li_xFeF₃ to LiF/Fe nanoparticles is slow leading to a kinetic limitation of the material. Considerable improvement was observed when raising the temperature (black and blue curves). After changing the discharge current back to its initial value of 17 mA⁻¹, the electrode (calendared, 55°C, red curve) lost 19 % of its initial capacity probably due to deterioration of the LiPF₆ electrolyte.

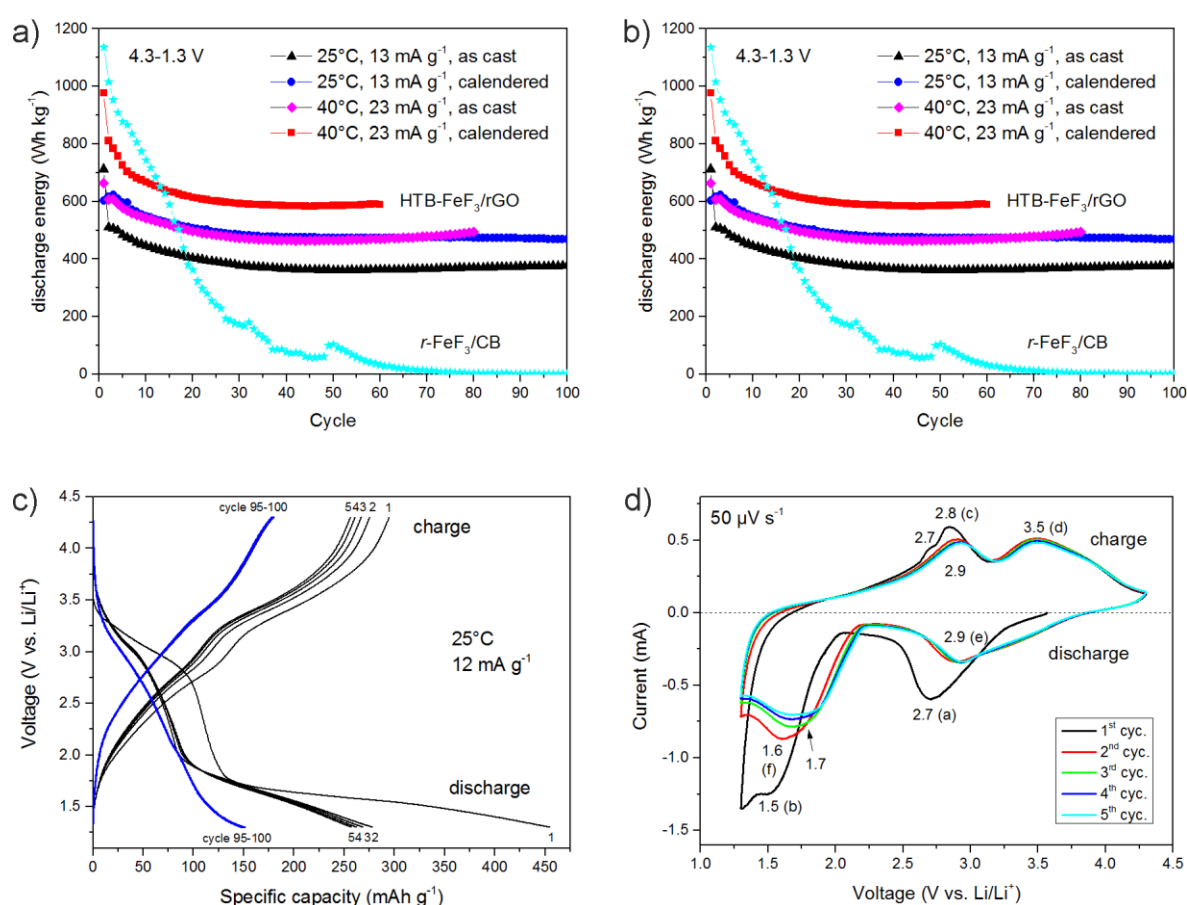


Figure 2: Electrochemical performance of HTB-FeF₃/rGO (**2**). a) Cyclic stability of as cast and calendared films in coin cells at 25°C and 40°C in comparison with FeF₃ ball milled with carbon black. b) Rate capability test of as cast and calendared films at 25°C and 55°C. The grey bar indicates the target of 700-800 Wh/kg on materials level.³ c) Galvanostatic profile and d) cyclovoltammogram of powder in a Swagelok cell.

The galvanostatic charge/discharge profile shown in Figure 2c resembles that of HTB-FeF₃ in the first cycle and amorphous FeF₃ in subsequent cycles as will be shown later. In the first cycle, there is a short plateau above 2.8 V where Li intercalation into the HTB-FeF₃ tunnel structure takes place^{15,16}

followed by a sloping region above 2 V and a long plateau due to conversion of HTB-Li_xFeF₃ into LiF and Fe nanoparticles. In summary, the overall conversion reaction can be written as $\text{FeF}_3 + 3\cdot\text{e}^- + 3\cdot\text{Li}^+ \rightleftharpoons \text{Fe}^0 + 3\cdot\text{LiF}$ leading to a theoretical capacity of 712 mAh g⁻¹ (1950 Wh kg⁻¹) for the 3 electron transfer. There is a large irreversible capacity loss of 135 mAh g⁻¹ in the first cycle due to formation of a solid electrolyte interface on the Li-metal anode³¹ or due to as yet unidentified reactions of the FeF₃ cathode with the electrolyte. After complete discharge, the HTB-FeF₃ is transformed into Fe metal nanoparticles embedded into an insulating matrix of LiF nanocrystallites.⁶ In subsequent cycles, the discharge plateau above 2.8 V is shortened considerably due to collapse of the HTB tunnel structure and subsequent formation of amorphous FeF₃, which has less capacity for Li storage than the HTB framework structure.

The CV diagram in Figure 2d clearly shows that the charge/discharge mechanism in the first cycle (black) differs from the storage mechanism in subsequent cycles (letters **a-f** correspond to regions defined in Figure 4). In the first cycle, the intercalation region **a** has a pronounced discharge peak with a maximum at 2.7 V. In subsequent cycles, peak **e** is shifted from 2.7 V to 2.9 V and is much broader compared to the first cycle indicating a solid solution or surface charge storage mechanism rather than an intercalation process. The conversion regimes **b** and **c** are characterised by a large voltage hysteresis of approximately 1.2 V due to the phase transformations.³²

Microstructure

The microstructure of HTB-FeF₃/rGO (**2**) was investigated using SEM, TEM and BET. The SEM image Figure 3a shows a large HTB-FeF₃/rGO particle with a textured surface covered by smaller HTB-FeF₃/rGO particles from top and side. EDX analysis (Figure S1, \$ESI) shows a strong overlap between O, C and F elemental maps indicating that HTB-FeF₃ particles are homogeneously coated by graphite oxide. The HR-TEM micrograph (Figure 3b) shows graphitic carbon layers rolled into onion-like structures. The graphitic layers have an interlayer spacing of $d = 3.5 \text{ \AA}$, which is in good agreement with the d -spacing of reduced graphene oxide³³ (but larger than $d = 3.356(4) \text{ \AA}$ reported for graphite³⁴). The enlarged interlayer distance shows that after oxidative/reductive treatment the natural graphite flakes are well exfoliated and the rGO layers contain lattice defects and residual oxygen groups on the surface which cause the layers to expand. Figure 3c shows HTB-FeF₃ nanoparticles (dark areas) embedded into carbon (spheres). The SAED pattern (inset) is in good agreement with the HTB-FeF₃·0.33H₂O structure.²⁹ A small portion of the HTB-FeF₃ particles shows mesoporosity with an average pore diameter of 6 nm (Figure 3d and Figure S2, \$ESI). However, the BET surface area of 20.1 m²/g and the cumulative pore volume of 0.04 cm³/g is small for a truly “porous” material indicating that the majority of HTB-FeF₃ particles exist as a dense solid phase (Figure S3, \$ESI). These dense particles are not accessible by N₂ molecules in BET measurements, but

are involved in Li diffusion process during intercalation and conversion reactions. The C_{1s} XPS spectrum of $r\text{-FeF}_3/\text{rGO}$ (**1**) (Figure S4, \S ESI) consists of the same carbon functionalities found for graphene oxide³⁵, but with reduced intensities of the C–O and C=O peaks indicating almost complete de-oxygenation by the reduction process. The combined TGA/DSC/MS analysis (Figure S5, \S ESI) shows that the $\text{HTB-FeF}_3/\text{rGO}$ (**2**) composite is thermally stable in air up to 300 °C.

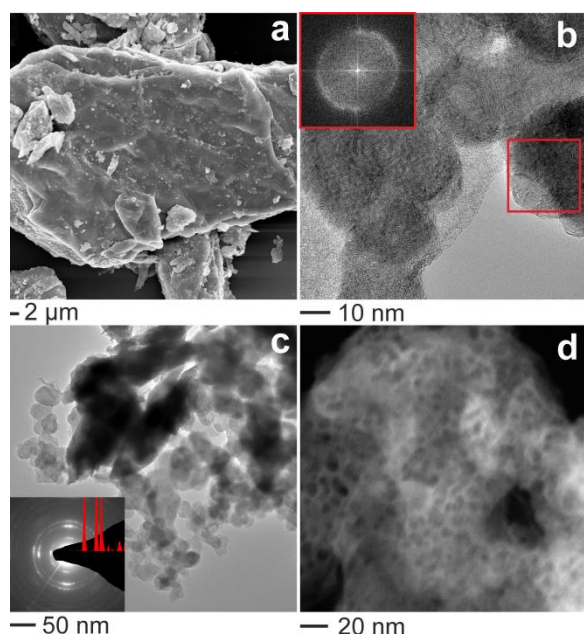


Figure 3: Morphology of $\text{HTB-FeF}_3/\text{rGO}$ (**2**) composite . a) SEM micrograph showing FeF_3 particles covered by layers of rGO carbon. b) HT-TEM micrograph of reduced graphene oxide (rGO) with SAED pattern of rGO ($d = 3.5 \text{ \AA}$) in inset. c) HR-TEM micrograph of FeF_3 particles (light grey areas) embedded into rGO carbon (dark areas). The SAED pattern (inset) shows a diffractogram matching the first three intense reflections of the HTB-FeF_3 structure (red bars). d) HAADF STEM image of a selected microporous FeF_3 particle with an average pore diameter of $d = 6 \text{ \AA}$.

Reaction mechanism

To investigate Fe oxidation state changes and the phases formed during intercalation and conversion of $\text{HTB-FeF}_3/\text{rGO}$, we collected simultaneous *in situ* synchrotron X-ray absorption and X-ray diffraction data and *ex situ* laboratory Mössbauer spectra at certain points in the 1st and beginning of 2nd cycle. Fe K-edge XANES and Mössbauer unambiguously determine the oxidation state of Fe, and are able to provide structural information when compared to literature data and theoretical simulations. On the other hand, XRD is able to detect changes in the long-range order as Li is intercalated. Figure 4 shows the voltage profile with points where *ex situ* Mössbauer spectra have been collected, the Fe concentration profile calculated from the Fe K-edge XANES spectra using principle component analysis, and a contour plot of X-ray diffraction data. All XANES spectra were

decomposed by the Principal Component Analysis (PCA) method into three subspectra, which correspond to Fe, FeF₂ and FeF₃ phases (Figure S6, §ESI). A summary of best guess structural phases determined with each technique is given in Table 2 and will be discussed in the following paragraphs.

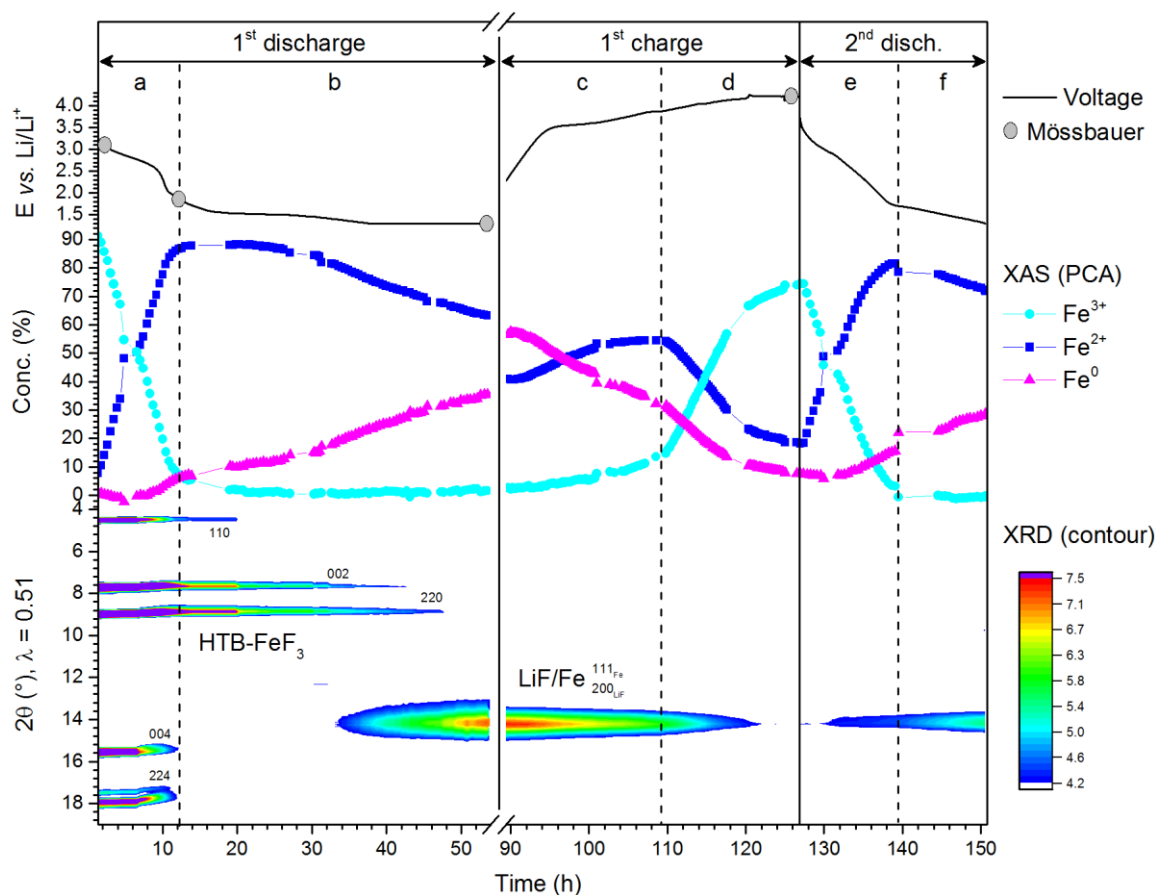


Figure 4: *In situ* XAS/XRD experiment of HTB-FeF₃/rGO (**3**) composite. Voltage profile during charge/discharge of the cell with grey circles indicating points where *ex situ* Mössbauer spectra were collected (top), PCA concentration profile of Fe, Fe²⁺ and Fe³⁺ components obtained from simultaneous decomposition of 260 Fe K-edge XANES spectra (middle) and XRD contour plot ($\lambda = 0.51 \text{ \AA}$) showing evolution of HTB-FeF₃, LiF and Fe phases during charge/discharge (bottom).

Before cycling, the as prepared HTB-FeF₃/rGO (**3**) composite consists mainly of HTB-FeF₃²⁹ with hexagonal tungsten bronze structure and large hexagonal channels along the *c*-axis (Figure 1). The channels are almost completely dehydrated (0.09 H₂O) and there is space to accommodate further Li atoms in the tunnels.¹⁶ The XAS spectrum shows a Fe³⁺ oxidation state and the spectrum resembles that of FeF₃. However, the local structures of *r*-FeF₃ and HTB-FeF₃ consist of very similar corner-sharing FeF₆ octahedra and cannot be easily distinguished by XAS. The Mössbauer spectrum (Figure 5) of as prepared HTB-FeF₃/rGO (**3**) composite shows two doublets, one with a larger quadrupole

splitting (QS) of 0.5(2) mm s⁻¹ and one with a smaller QS of 0.22(2) mm s⁻¹ (Table 3). The large Fe³⁺ doublet is in good agreement with the fully hydrated structure HTB-FeF₃·0.33H₂O with 1/3 water in the channels.²⁹ The small Fe³⁺ doublet may be due to the partial removal of H₂O molecules from the channels and, as has been observed by XRD, represents the partially dehydrated HTB-FeF₃ structure reported by Calage et al.³⁶ The Mössbauer spectrum also indicates the presence of a small amount of *r*-FeF₃ (3% ra) with a large magnetic hyperfine splitting of 40.4 T³⁷ in agreement with the XRD refinement (Table 1). Additionally, there is an Fe²⁺ component (7% ra) with an isomer shift of 1.14(2) mm s⁻¹ and a large QS of 2.56 mm s⁻¹. These parameters suggest some form of nanocrystalline FeF₂.³⁸ It is known that *r*-FeF₃ is not stable under high-energy ball milling conditions and tends to partially reduce to FeF₂.³⁹ However, the particle size of FeF₂ must be very small as no additional macroscopic FeF₂ phase was identified in the XRD pattern.

Table 2: Best guess structural phases found in HTB-FeF₃/rGO (**3**) composite during cycling. Numbers in parenthesis: PCA concentrations, XRD phase fraction in wt.% and Mössbauer relative area.

	XAS	XRD	Mössbauer
as prepared	Fe ³⁺ (91) Fe ²⁺ (8) Fe ⁰ (1)	HTB-FeF ₃ (77) <i>r</i> -FeF ₃ (21) WC (2)	FeF ₃ ·0.33H ₂ O (62) HTB-FeF ₃ (28) <i>n</i> -FeF ₂ , bulk (7) <i>r</i> -FeF ₃ (3)
dc 3.0 V	Fe ³⁺ (78) Fe ²⁺ (22)	HTB-Li _x FeF ₃	Fe ³⁺ (58) Fe ²⁺ (42)
dc 1.9 V	Fe ²⁺ (86) Fe ³⁺ (8) Fe ⁰ (6)	HTB-Li _x FeF ₃	Fe ²⁺ (80) Fe ³⁺ (20)
dc 1.3 V	Fe ⁰ (57) Fe ²⁺ (41) Fe ³⁺ (2)	LiF Fe	<i>n</i> -Fe (56) Fe ²⁺ (23) Fe ³⁺ (21)
ch 4.3 V	Fe ³⁺ (74) Fe ²⁺ (19) Fe ⁰ (8)		<i>α</i> -FeF ₃ (75) <i>n</i> -FeF ₂ , int. (17) <i>n</i> -FeF ₂ , bulk (8)

r: rhombohedral; *n*: nanocrystalline; *α*: amorph

During discharge (region **a**, **b**), Li is intercalated into the HTB-FeF₃ structure up to a voltage of 2.0 V as has been observed previously,¹⁶ and is subsequently transformed into LiF and Fe nanoparticles when discharging to the cutoff voltage of 1.3V. During the Li intercalation process (**a**), reflections of HTB-FeF₃ shift to lower 2θ values with a corresponding unit cell volume expansion of approx. 5 % (Figure 6). The cell expansion is fairly linear up the end of the voltage plateau at approx. 2.5 V, which is in agreement with a topotactical Li-insertion process described by Vegard's law.⁴⁰ The XAS spectra of the Li-intercalation process (Figure 7a) show four isosbestic points characteristic for a two phase mixture consisting of HTB-FeF₃ and HTB-Li_xFeF₃. At the end of the intercalation process, the Fe³⁺ peak

(inset Figure 7a) has almost entirely disappeared and the iron atoms are mainly in a Fe^{2+} state corresponding to a fully intercalated $\text{HTB-Li}_x\text{FeF}_3$ structure. From the PCA concentration profile (Figure 4) we calculated that $x = 0.95$ Li at the end of the intercalation process, which is much larger than the maximum of 0.66 Li for $\text{HTB-FeF}_3 \cdot 0.33\text{H}_2\text{O}$ found by the Maier group.¹⁶ We think this is possible because in the partially dehydrated $\text{HTB-FeF}_3 \cdot 0.09\text{H}_2\text{O}$ structure, there is more room for Li atoms available compared to $\text{HTB-FeF}_3 \cdot 0.33\text{H}_2\text{O}$ with 1/3 of the channels already occupied by water molecules. The Mössbauer spectra (Figure 5) collected in the middle and end of region (a) (3.0 V and 1.9 V, respectively), show a number of Fe^{2+} and Fe^{3+} doublets, which cannot be assigned unambiguously to any known iron fluoride phases to date. We assume that these doublets are due to Fe environments in partially lithiated $\text{HTB-Li}_x\text{FeF}_3$. The Fe^{2+} doublets show a remarkable similarity with nanocrystalline FeF_2 with one doublet for Fe atoms located at the interface of FeF_2 particles and one doublet for Fe atoms in the bulk.³⁸ However, there remains doubt if there is an additional phase transition from $\text{HTB-Li}_x\text{FeF}_3$ to $n\text{-FeF}_2$ before conversion because a) the quadrupole splitting (QS) of the Fe^{2+} doublets observed in our composite is slightly smaller than that observed for $n\text{-FeF}_2$ (Table 3) and b) to date there is no comparable Mössbauer data for $\text{HTB-Li}_x\text{FeF}_3$ available in the literature. The Fe^{3+} doublets in the 3.0 V and 1.9 V spectra have an enlarged QS compared to pristine HTB-FeF_3 ($0.58\text{-}0.64 \text{ mm s}^{-1}$) probably due to additional Li atoms in the channels.

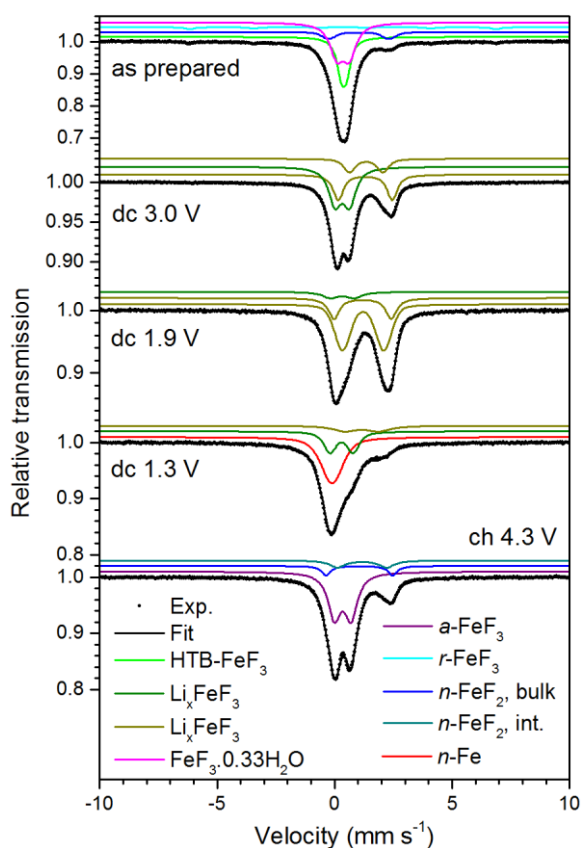


Figure 5: Mössbauer spectra of as prepared HTB-FeF₃/rGO (**3**) composite, discharged to 3.0 V, 1.9 V and 1.3 V and charged to 4.3 V. The experimental spectrum is given as black dots and the total fit as a black line. Components of the fit are shown as coloured lines above the spectrum. The relative shift is given to α -Fe.

Table 3: *Ex situ* Mössbauer parameters of HTB-FeF₃/rGO (**3**) during charge/discharge. Isomer shift (IS), quadrupole splitting (QS), Lorentzian linewidth (Γ) and hyperfine splitting (BHF). IS relative to α -Fe. Reported values for known iron fluorides are given for comparison.

	IS mm s ⁻¹	QS mm s ⁻¹	Γ mm s ⁻¹	BHF T	Area %
as prepared	0.47(1)	0.54(18)	0.67(10)	–	61.9
	0.50(2)	0.22(2)	0.46(7)	–	28.0
	1.14(2)	2.56(3)	0.4	–	7.0
	0.46(1)	0.01(3)	0.41(5)	40.4(1)	3.0
dc 3.0 V	0.33(3)	0.62(5)	0.598(6)	–	57.8
	1.305(5)	2.300(9)	0.49(1)	–	28.0
	1.35(8)	1.4(2)	0.45(5)	–	14.2
dc 1.9 V	1.321(2)	1.76(2)	0.31(4)	–	46.0
	1.302(2)	2.434(6)	0.56(2)	–	33.9
	0.43(1)	1.02(1)	0.81(3)	–	20.0
dc 1.3 V	0	–	0.70(2)	–	55.5
	1.27(4)	1.45(7)	1.10(3)	–	23.3
	0.405(4)	0.979(6)	0.5	–	21.2
ch 4.3 V	0.456(2)	0.709(4)	0.649(2)	–	75.0
	1.279(7)	2.11(2)	0.78(2)	–	17.3
	1.167(4)	2.83(1)	0.44(2)	–	7.7
FeF ₃ ·0.33 H ₂ O ²⁹	0.439(2)	0.640(4)	0.50(1)	–	–
HTB-FeF ₃ ³⁶	0.400(5) ^a	0.58(2)	0.49(4)	–	61(5)
	0.419(5)	0.23(2)	0.36(4)	–	39(5)
<i>r</i> -FeF ₃ ³⁷	0.474(6)	0.05(1)	0.246	40.4(2)	–
α -FeF ₃ ⁴¹	0.48	0.58	0.45	–	–
FeOF ⁴²	0.397	1.18	–	–	–
FeF ₂ ⁴³	1.37	2.78	0.23	–	–
<i>n</i> -FeF ₂ ³⁸	1.289 bulk	2.733	0.352	–	75
	1.267 int.	1.968	0.550	–	25

^a IS converted from 100 K to 300

^b *r*: rhombohedral; *n*: nanocrystalline; *a*: amorphous

In the conversion regime (**b**) below 2.0 V, HTB-Li_xFeF₃ converts to LiF/Fe nanoparticles as can be clearly seen by the appearance of a broad LiF/Fe peak in the XRD contour plot Figure 4 and the *in situ* XAS spectra (Figure 7b). The XAS spectra show another set of isosbestic points and a growing Fe⁰ peak (inset) indicating two phases in equilibrium (LiF cannot be seen by Fe-K edge XAS). The PCA concentration profile (Figure 4) shows that the cell after full discharge contains 63 % Fe²⁺, 36 % Fe⁰ and no Fe³⁺. This clearly shows that the conversion of HTB-Li_xFeF₃ to LiF/Fe was not complete and is much slower compared to fast Li-intercalation process in the beginning of discharge. A second cell,

which was discharged to 1.3 V prior to the synchrotron experiment, had a much higher Fe content of 57 % Fe⁰ and 41 % Fe²⁺ at the end of discharge and this cell was used in subsequent charge/discharge cycles (c-f). The *ex-situ* Mössbauer spectrum (Figure 5) collected after full discharge at 1.3 V shows a Fe⁰ singlet due to superparamagnetic Fe nanoparticles^{44,45} and two doublets for Fe²⁺ and Fe³⁺, respectively, which are due to unreacted HTB-Li_xFeF₃.

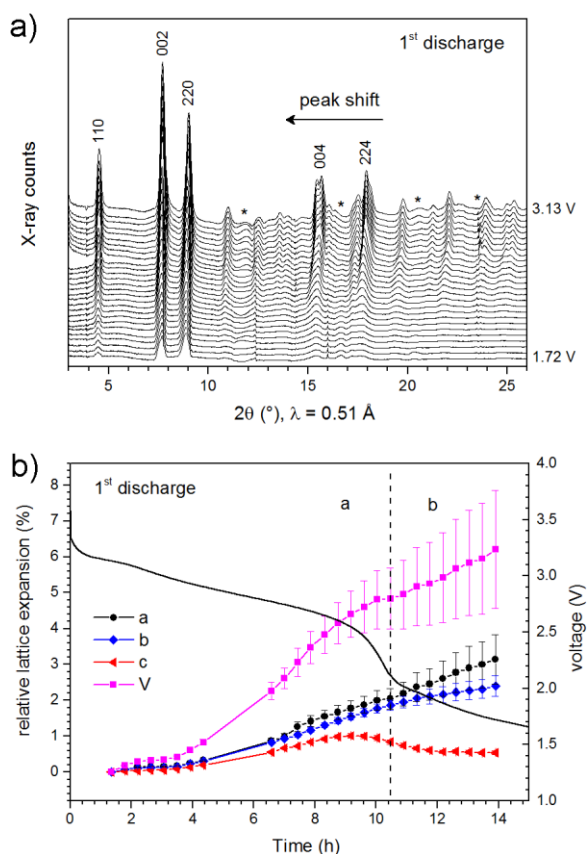


Figure 6: a) *In situ* X-ray diffraction patterns of HTB-FeF₃/rGO (**3**) composite collected during 1st discharge showing a peak shift due to Li intercalation into HTB-FeF₃. Li reflections (*) have been excluded for clarity. b) Relative lattice expansion calculated from refined lattice parameters of HTB-FeF₃ phase.

During charge (c, d), the LiF/Fe nanoparticles transform reversibly to FeF₂ and FeF₃.⁴⁴ To the best of our knowledge, it has not been investigated which FeF₂ or FeF₃ polymorph will form when charging a previously discharged HTB-FeF₃ composite rather than the better investigated *r*-FeF₃/carbon composites. The XRD diffraction data (Figure 4) did not show any new phases during charge indicating that the FeF₂ and FeF₃ particles are nanocrystalline with domain sizes below the coherent X-ray scattering length. However, the transformation of Fe into FeF₂ and FeF₃ is clearly visible in the PCA concentration profile. In the beginning of the charge process (c), the amount of Fe²⁺ increases

indicating formation of FeF_2 , and above 3.87 V (region **d**) the Fe^{2+} concentration decreases fast with concomitant oxidation and formation of FeF_3 . The Mössbauer spectrum collected after full charge at 4.3 V (Figure 5) shows a large Fe^{3+} doublet, which is in good agreement with amorphous FeF_3 . Due to the very small particles we do not observe a hyperfine splitting as would be expected for ferromagnetic *r*- FeF_3 . The spectrum also contains two Fe^{2+} doublets, one with a small QS of 2.11 mm s^{-1} and one with a large QS of 2.83 mm s^{-1} , which are in good agreement with nanocrystalline FeF_2 (Table 3). This is evidence that the charge process does not go *via* the HTB-framework structure forming HTB- Li_xFeF_3 , but rather through the formation of rutile FeF_2 and rhombohedral FeF_3 phases as has been observed for other *r*- FeF_3 /carbon composites.

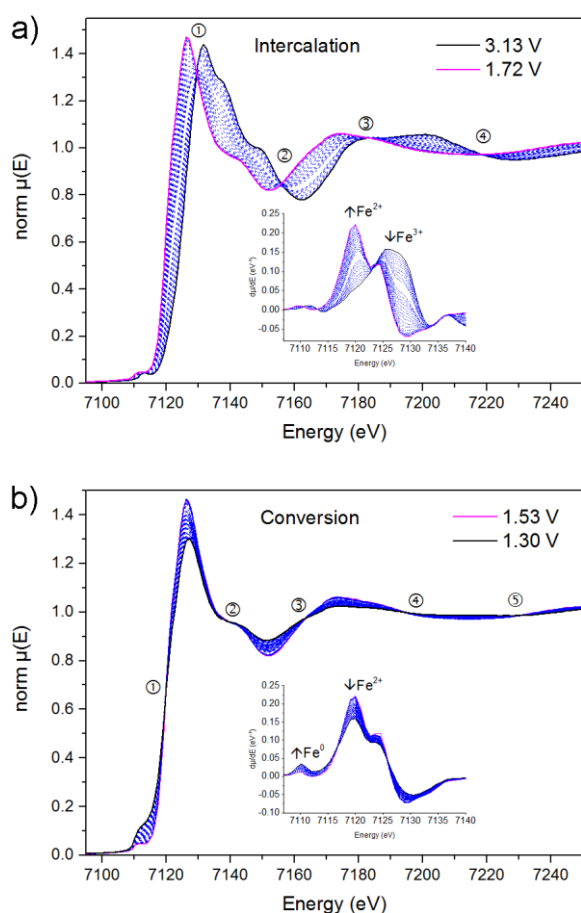


Figure 7: *In situ* Fe K-edge XAS spectra of HTB- FeF_3 /rGO (**3**) showing a) Li-intercalation with characteristic isosbestic points (marked with numbers 1-4). The inset shows the derivative spectra with increasing Fe^{2+} and decreasing Fe^0 peak intensity. b) Conversion of HTB- FeF_3 into LiF and Fe indicated by a second set of isosbestic points.

Conclusion

We have synthesised HTB-FeF₃/rGO (and *r*-FeF₃/rGO) composite materials as a high energy cathode for Li-ion batteries from graphene oxide suspension and commercial FeF₃ using a HF-free and scalable preparation method. The composites consist of a phase mixture of HTB-FeF₃ and *r*-FeF₃ polymorphs depending on ball milling conditions and temperature during reduction process. HTB-FeF₃/rGO composites show a stable discharge capacity of 400-450 mAh/g at 55°C vs. Li metal anode and a remarkably good cycle stability over 100 cycles. The good cycle performance was attributed to the microstructure, which consists of FeF₃ particles covered entirely by reduced graphene oxide layers. The stable carbon coating of hygroscopic FeF₃ particles permits the preparation of high quality electrodes without the need of moisture protection in ambient air and maintains electronic as well as Li ionic conductivity during prolonged cycling. The detailed reaction mechanism was investigated using a combination of *in situ* XAS, XRD and *ex situ* Mössbauer spectroscopy. Upon discharge, Li is inserted fast into the HTB-FeF₃ tunnel structure followed by a slow conversion reaction to LiF/Fe nanoparticles. Upon charge, LiF/Fe is slowly converted back to rutile FeF₂ and rhombohedral FeF₃ phases without reformation of the HTB-FeF₃ framework. The HTB-FeF₃/rGO material is able to deliver a high specific energy of 700-800 Wh/kg at elevated temperature and slow rates, but the energy density is reduced at higher rates due to kinetic limitations of the conversion reaction. A solid or liquid electrolyte suitable for cycling the material above 100°C might be a way to improve the energy density and rate capability of HTB-FeF₃/rGO significantly.

Acknowledgements

The authors would like to thank the European Synchrotron Radiation Facility (ESRF) for granting beam time for the *in situ* XAS/XRD experiment. We also thank C. Ly for providing ICP-OES analytical service at the Karlsruhe Institute of Technology (FM-VEA). A. G. and V. S. would like to thank the Ministry of Education and Science of Russia for the financial support (agreement № 14.587.21.0002, identifier RFMEFI58714X0002). Financial support by EU-RTD "Hi-C" (Novel *in situ* and *in operando* techniques for characterization of interfaces in electrochemical storage systems") in the 7th FP, grant agreement no. 608575 is gratefully acknowledged.

Supporting Information Available: Synthesis of aqueous graphene oxide and FeF₃/rGO composite material, electrode preparation, EDX maps, FeF₃ pore size distribution, N₂ physisorption isotherm, XPS, TGA/DSC/MS analysis, Fe K-edge XANES PCA analysis and reference spectra. This material is available free of charge via the Internet at <http://pubs.acs.org>

References

- (1) Fichtner, M. Conversion Materials for Hydrogen Storage and Electrochemical applications— Concepts and Similarities. *J. Alloys Compd.* **2011**, *509*, S529–S534.
- (2) DOE Annual Merit Review 2012, <http://www.annualmeritreview.energy.gov>.
- (3) Andre, D.; Kim, S.-J.; Lamp, P.; Lux, S. F.; Maglia, F.; Paschos, O.; Stiaszny, B. Future Generations of Cathode Materials: An Automotive Industry Perspective. *J. Mater. Chem. A* **2015**, *3*, 6709–6732.
- (4) Fichtner, M. Konversionsmaterialien für die Energiespeicherung. *Chemie unserer Zeit* **2013**, *47* (4), 230–238.
- (5) Cabana, J.; Monconduit, L.; Larcher, D.; Palacín, M. R. Beyond Intercalation-Based Li-Ion Batteries: The State of the Art and Challenges of Electrode Materials Reacting through Conversion Reactions. *Adv. Mater.* **2010**, *22* (35), E170–E192.
- (6) Wang, F.; Yu, H.-C.; Chen, M.-H.; Wu, L.; Pereira, N.; Thornton, K.; Van der Ven, A.; Zhu, Y.; Amatucci, G. G.; Graetz, J. Tracking Lithium Transport and Electrochemical Reactions in Nanoparticles. *Nat. Commun.* **2012**, *3*, 1201.
- (7) Li, H.; Balaya, P.; Maier, J. Li-Storage via Heterogeneous Reaction in Selected Binary Metal Fluorides and Oxides. *J. Electrochem. Soc.* **2004**, *151* (11), A1878.
- (8) Conte, D. E.; Pinna, N. A Review on the Application of iron(III) Fluorides as Positive Electrodes for Secondary Cells. *Mater. Renew. Sustain. Energy* **2014**, *3* (4), 37.
- (9) Badway, F.; Cosandey, F.; Pereira, N.; Amatucci, G. G. Carbon Metal Fluoride Nanocomposites. *J. Electrochem. Soc.* **2003**, *150* (10), A1318–A1327.
- (10) Zhao, X.; Hayner, C. M.; Kung, M. C.; Kung, H. H. Photothermal-Assisted Fabrication of Iron Fluoride-Graphene Composite Paper Cathodes for High-Energy Lithium-Ion Batteries. *Chem. Commun.* **2012**, *48* (79), 9909–9911.
- (11) Liu, J.; Wan, Y.; Liu, W.; Ma, Z.; Ji, S.; Wang, J.; Zhou, Y.; Hodgson, P.; Li, Y. Mild and Cost-Effective Synthesis of Iron Fluoride–graphene Nanocomposites for High-Rate Li-Ion Battery Cathodes. *J. Mater. Chem. A* **2013**, *1* (6), 1969.
- (12) Ma, R. G.; Lu, Z. G.; Wang, C. D.; Wang, H. E.; Yang, S. L.; Xi, L. J.; Chung, J. C. Y. Large-Scale Fabrication of Graphene-Wrapped FeF₃ Nanocrystals as Cathode Materials for Lithium Ion Batteries. *Nanoscale* **2013**, *5* (14), 6338–6343.
- (13) Chu, Q.; Xing, Z.; Ren, X.; Asiri, A. M.; Al-Youbi, A. O.; Alamry, K. A.; Sun, X. Reduced Graphene Oxide Decorated with FeF₃ Nanoparticles: Facile Synthesis and Application as a High Capacity Cathode Material for Rechargeable Lithium Batteries. *Electrochim. Acta* **2013**, *111*, 80–85.
- (14) Ma, R.; Dong, Y.; Xi, L.; Yang, S.; Lu, Z.; Chung, C. Fabrication of LiF/Fe/Graphene Nanocomposites as Cathode Material for Lithium-Ion Batteries. *ACS Appl. Mater. Interfaces* **2013**, *5* (3), 892–897.

- (15) Li, C.; Gu, L.; Tsukimoto, S.; van Aken, P. a; Maier, J. Low-Temperature Ionic-Liquid-Based Synthesis of Nanostructured Iron-Based Fluoride Cathodes for Lithium Batteries. *Adv. Mater.* **2010**, *22* (33), 3650–3654.
- (16) Li, C.; Gu, L.; Tong, J.; Tsukimoto, S.; Maier, J. A Mesoporous Iron-Based Fluoride Cathode of Tunnel Structure for Rechargeable Lithium Batteries. *Adv. Funct. Mater.* **2011**, *21* (8), 1391–1397.
- (17) Li, C.; Gu, L.; Tong, J.; Maier, J. Carbon Nanotube Wiring of Electrodes for High-Rate Lithium Batteries Using an Imidazolium-Based Ionic Liquid Precursor as Dispersant and Binder: A Case Study on Iron Fluoride Nanoparticles. *ACS Nano* **2011**, *5* (4), 2930–2938.
- (18) Li, C.; Mu, X.; van Aken, P. A.; Maier, J. A High-Capacity Cathode for Lithium Batteries Consisting of Porous Microspheres of Highly Amorphized Iron Fluoride Densifi Ed from Its Open Parent Phase. *Adv. Energy Mater.* **2013**, *3* (1), 113–119.
- (19) Li, C.; Yin, C.; Mu, X.; Maier, J. Top-down Synthesis of Open Framework Fluoride for Lithium and Sodium Batteries. *Chem. Mater.* **2013**, *25* (6), 962–969.
- (20) Wang, F.; Kim, S.; Seo, D.; Kang, K.; Wang, L.; Su, D.; Vajo, J. J.; Wang, J.; Graetz, J. Ternary Metal Fluorides as High-Energy Cathodes with Low Cycling Hysteresis. *Nat. Commun.* **2015**, *6*, 1–9.
- (21) Pohl, A. H.; Guda, A. A.; Shapovalov, V. V.; Witte, R.; Das, B.; Scheiba, F.; Rothe, J.; Soldatov, A. V.; Fichtner, M. Oxidation State and Local Structure of a High-Capacity LiF/Fe(V₂O₅) Conversion Cathode for Li-Ion Batteries. *Acta Mater.* **2014**, *68*, 179–188.
- (22) Rourke, J. P.; Pandey, P. a; Moore, J. J.; Bates, M.; Kinloch, I. a; Young, R. J.; Wilson, N. R. The Real Graphene Oxide Revealed: Stripping the Oxidative Debris from the Graphene-like Sheets. *Angew. Chem. Int. Ed. Engl.* **2011**, *50* (14), 3173–3177.
- (23) Coelho, A. A. TOPAS-Academic V4.1. Coelho Software: Brisbane, Australia 2007.
- (24) Hammersley, A. P.; Svensson, S. O.; Hanfland, M.; Fitch, A. N.; Hausermann, D. Two-Dimensional Detector Software: From Real Detector to Idealised Image or Two-Theta Scan. *High Press. Res.* **1996**, *14* (4-6), 235–248.
- (25) Beale, A. M.; Le, M. T.; Hoste, S.; Sankar, G. A Time Resolved in Situ Investigation into the Formation of Bismuth Molybdate Catalysts Prepared by Spray-Dried Methods. *Solid State Sci.* **2005**, *7* (10), 1141–1148.
- (26) Coulston, G. W. The Kinetic Significance of V⁵⁺ in N-Butane Oxidation Catalyzed by Vanadium Phosphates. *Science* **1997**, *275* (5297), 191–193.
- (27) Smolentsev, G.; Soldatov, a. V. FitIt: New Software to Extract Structural Information on the Basis of XANES Fitting. *Comput. Mater. Sci.* **2007**, *39* (3), 569–574.
- (28) Leblanc, M.; Pannetier, J.; Ferey, G.; de Pape, R. Single Crystal Refinement of the Structure of Rhombohedral FeF₃. *Rev. Chim. Miner.* **1985**, *22*, 107–114.

- (29) Leblanc, M.; Ferey, G.; Chevallier, P.; Calage, Y.; De Pape, R. Hexagonal Tungsten Bronze-Type FeIII Fluoride: $(\text{H}_2\text{O})_{0.33}\text{FeF}_3$; Crystal Structure, Magnetic Properties, Dehydration to a New Form of Iron Trifluoride. *J. Solid State Chem.* **1983**, *47* (1), 53–58.
- (30) Täubert, C.; Fleischhammer, M.; Wohlfahrt-Mehrens, M.; Wietelmann, U.; Buhrmester, T. LiBOB as Electrolyte Salt or Additive for Lithium-Ion Batteries Based on $\text{LiNi}_{0.8}\text{Co}_{0.15}\text{Al}_{0.05}\text{O}_2/\text{Graphite}$. *J. Electrochem. Soc.* **2010**, *157* (6), A721.
- (31) Illig, J. *Physically Based Impedance Modelling of Lithium-Ion Cells*; KIT Scientific Publishing: Karlsruhe, 2014.
- (32) Ko, J. K.; Wiaderek, K. M.; Pereira, N.; Kinnibrugh, T. L.; Kim, J. R.; Chupas, P. J.; Chapman, K. W.; Amatucci, G. G. Transport, Phase Reactions, and Hysteresis of Iron Fluoride and Oxyfluoride Conversion Electrode Materials for Lithium Batteries. *ACS Appl. Mater. Interfaces* **2014**, *6* (14), 10858–10869.
- (33) Huh, S. H.; Choi, S.-H.; Ju, H.-M.; Kim, D.-H. Properties of Interlayer Thermal Expansion of 6-Layered Reduced Graphene Oxide. *J. Korean Phys. Soc.* **2014**, *64* (4), 615–618.
- (34) Trucano, P.; Chen, R. Structure of Graphite by Neutron Diffraction. *Nature*. 1975, pp 136–137.
- (35) Stankovich, S.; Piner, R. D.; Chen, X.; Wu, N.; Nguyen, S. T.; Ruoff, R. S. Stable Aqueous Dispersions of Graphitic Nanoplatelets via the Reduction of Exfoliated Graphite Oxide in the Presence of Poly(sodium 4-Styrenesulfonate). *J. Mater. Chem.* **2006**, *16* (2), 155.
- (36) Calage, Y.; Leblanc, M.; Ferey, G.; Varret, F. Mössbauer Investigation of Hexagonal Tungsten Bronze Type FeIII Fluorides: $(\text{H}_2\text{O})_{0.33}\text{FeF}_3$ and Anhydrous FeF_3 . *J. Magn. Magn. Mater.* 1984, pp 195–203.
- (37) Wertheim, G. K.; Guggenheim, H. J.; Buchanan, D. N. E. Sublattice Magnetization in FeF_3 near the Critical Point. *Phys. Rev.* **1968**, *169* (2), 465–470.
- (38) Ramasamy, S.; Jiang, J.; Gleiter, H.; Birringer, R.; Gonser, U. Investigation of Nanocrystalline FeF_2 by Mössbauer Spectroscopy. *Solid State Commun.* **1990**, *74* (8), 851–855.
- (39) Matteazzi, P.; Caër, G. Le. Exchange Reaction Milling in Iron Nitrides, Fluorides and Carbides. *J. Alloys Compd.* **1992**, *187* (2), 305–315.
- (40) Denton, A. R.; Ashcroft, N. W. Vegards Law. *Phys. Rev. A* **1991**, *43* (6), 3161–3164.
- (41) Grenèche, J. M.; Varret, F. Mössbauer Effect Studies of Iron Fluorides. In *Mössbauer Spectroscopy Applied to Magnetism and Materials Science*; Long, G. J., Grandjean, F., Eds.; 1993; pp 161–203.
- (42) Chappert, J.; Portier, J. Effet Mössbauer Dans FeOF . *Solid State Commun.* May 1966, pp 185–188.
- (43) Greenwood, N. N.; Howe, A. T.; Ménil, F. Mössbauer Studies of Order and Disorder in Rutile and Trirutile Compounds Derived from FeF_2 . *J. Chem. Soc. A Inorganic, Phys. Theor.* **1971**, 2218.

- (44) Wang, F.; Robert, R.; Chernova, N. a; Pereira, N.; Omenya, F.; Badway, F.; Hua, X.; Ruotolo, M.; Zhang, R.; Wu, L.; Volkov, V.; Su, D.; Key, B.; Whittingham, M. S.; Grey, C. P.; Amatucci, G. G.; Zhu, Y.; Graetz, J. Conversion Reaction Mechanisms in Lithium Ion Batteries: Study of the Binary Metal Fluoride Electrodes. *J. Am. Chem. Soc.* **2011**, *133* (46), 18828–18836.
- (45) Christensen, P. H.; Moerup, S.; Niemantsverdriet, J. W. Particle Size Determination of Superparamagnetic α -Fe in Carbon-Supported Catalysts by in Situ Moessbauer Spectroscopy. *J. Phys. Chem.* **1985**, *89* (23), 4898–4900.